Numerical simulation on onset characteristics of traveling-wave thermoacoustic engines based on a time-domain network model

K. Wang, D.M. Sun[*], J. Zhang, J. Zou, K. Wu, L.M. Qiu, Z.Y. Huang

Faculty of Engineering, Zhejiang University, Hangzhou 310027, PR China

Abstract

Onset characteristics of thermoacoustic engines are of great importance for understanding the internal working mechanisms of thermoacoustic conversion. A one-dimensional time-domain network model for predicting the onset characteristics of traveling-wave thermoacoustic engines with helium as working gas is built. The acoustic resistance, inertance, compliance, and thermal-relaxation effects of all the acoustic components are included. The viscous and heat transfer terms in the time-domain governing equations of the acoustic tubes and the heat exchangers are deduced from the frequency-domain linear thermoacoustic theory. Combining the time-domain governing equations of the regenerator, numerical simulations of the whole onset process are then conducted in a wide operating condition range. The complete dynamic pressure wave evolution processes are simulated successfully. It is shown that a steady standing-wave acoustic field forms in almost all parts of the traveling-wave thermoacoustic engine except for the regenerator area. Onset temperature, operating frequency, and quality factor are calculated with a relatively high accuracy. The thermal relaxation effects in the regenerator are found to have a remarkable impact on the onset characteristics, especially at high mean pressures. It is also shown that the experimental damping temperature is closer to the calculated onset temperature than the experimental onset temperature. Furthermore, the reasonable distributions of the pressure and volume flow rate and the phase relationship between them in the whole system are obtained and analyzed.

Keywords: thermoacoustic, onset, regenerator, acoustic, time-domain

1. Introduction

Thermoacoustic engines are capable of converting thermal energy into acoustic power with comparable efficiencies as that of conventional heat engines [1]. Due to the unique feature of no moving mechanical components, thermoacoustic engines have great advantages of simple structure, high reliability, and low costs. Thermoacoustic engines can be classified into standing-wave [2-10] and traveling-wave types [11-14] based on the differences in configuration and working mechanism. Standing-wave thermoacoustic engines have simpler structures but lower efficiencies due to the intrinsically imperfect heat transfer in the stacks. The energy conversion process in a traveling-wave thermoacoustic engine takes place reversibly based on a good thermal contact between gas and porous solids in the regenerator. As a result, traveling-wave thermoacoustic engines work more efficiently and are more promising in the practical applications compared to their standing-wave counterparts [12,15].

---

[*] Corresponding authors. Tel/Fax: +86-571-87952769 (D. M. Sun)
  E-mail address: sundaming@zju.edu.cn (D. M. Sun)

During the past decades, great efforts have been made to reveal the working mechanisms and improve the performance of thermoacoustic engines. Linear thermoacoustic theory [16] is now widely adopted to design thermoacoustic engines and predict the performances of them operating at steady states. However, as the control equations are linearized in the frequency-domain, transient processes in thermoacoustic systems cannot be simulated by linear thermoacoustic theory, which obscures important time-domain information of thermoacoustic effect.

Onset process indicates the spontaneous transition of the working gas in a thermoacoustic engine from the stationary to a periodic oscillating state when a sufficient temperature gradient is established along the stack or regenerator. The pressure amplitude in the system then grows until it gets saturated when an energy balance between acoustic generation and dissipation is reached. The nonlinear behaviors of thermoacoustic engines in onset process are of great importance for better understanding thermoacoustic phenomenon. Besides, onset temperature, i.e. the lowest heating temperature required to excite the oscillations, is also an important parameter because it determines the lowest grade of heat that a thermoacoustic engine can harvest.

Previous numerical calculations mainly focused on the onset characteristics of standing-wave thermoacoustic engines [17-26] due to the much simpler configuration and earlier invention of them. However, much less numerical work has been done to characterize the onset process of traveling-wave thermoacoustic engines. Lycklama et al. [27] and Yu et al. [28] performed axisymmetric 2D simulations of traveling-wave thermoacoustic engines by using commercial computational fluid dynamics (CFD) softwares in 2005 and 2007, respectively. Onset temperature and nonlinear pressure amplification were obtained. However, a special topological transformation should be made to turn the original configuration into an axisymmetric 2D model, which introduces the extra difficulties for the modeling and adds uncertainty for the prediction of onset parameters. The long computational time and huge resources required by CFD methods are also big problems. In 2009, de Waele [29] proposed a simplified thermodynamic model for the simulation of onset condition and transient effects in traveling-wave thermoacoustic engines. All components were treated by lumped parameter method and losses in the pipes were represented by an arbitrarily given resistance load, which diverges much from the real system. Up to now, it still lacks an efficient and accurate time-domain model for the simulation of the onset and transient characteristics of traveling-wave thermoacoustic engines.

In this paper, a one-dimensional time-domain thermoacoustic network model capable of calculating the onset temperature and the simulation of dynamic onset process is proposed. Nearly all the thermoacoustic effects, including resistance, inertance, compliance, and thermal-relaxation, are considered in the acoustic tubes and the heat exchangers. Effects of the thermal relaxation effects in the regenerator on the onset characteristics are studied with two different treatments of the continuity equations for the regenerator. The complete time-domain differential equations for an entire traveling-wave thermoacoustic engine are first given, and the discretization method as well as the algorithm are further presented in detail. The overall evolutionary onset process, the onset temperature, the operating frequency and the quality factor are then obtained, which are then verified by experimental results.

2. Mathmatical model

2.1. Geometry parameters

Fig. 1 shows the schematic diagram of the traveling-wave thermoacoustic engine used in the

model and the experiments [12]. The engine is composed of a hot heat exchanger (HHX), a stacked-screen regenerator, a main ambient heat exchanger (AHX), a secondary ambient heat exchanger (2nd AHX) and a few tube components. As the oscillating flow generates a second order mean flow around the loop, i.e. Gedeon streaming, which is harmful to the performance, an elastic membrane is placed above the main AHX to totally suppress it. The main AHX is of shell-and-tube type with working gas flowing inside the thin tubes. The total number and inner diameter of the tubes are 301 and 2 mm, respectively. The regenerator is filled with stainless steel screens with a porosity of 0.777 and a hydraulic radius of 52.4 μm. The HHX is of fin type with a porosity of 0.361 and the fin spacing is 1 mm. The 2nd AHX is also of shell-and-tube type; the inner diameter of gas tubes is 3 mm; the total porosity is 0.179. The main geometric parameters of the components are given in Table 1.
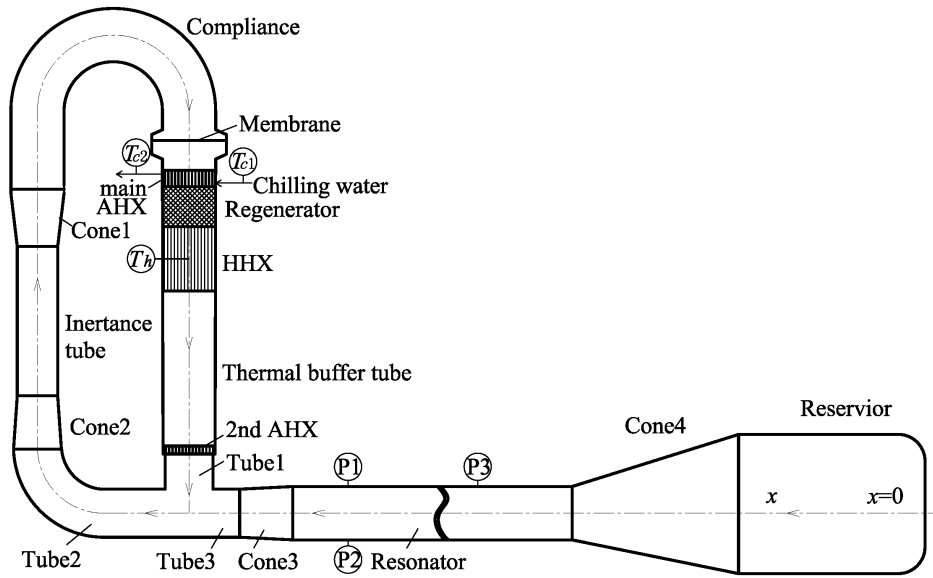

FIG. 1. Schematic diagram of traveling-wave thermoacoustic engine.

2.2. Governing equations

The model in this study is based on the following assumptions and simplifications:

1) The period of pressure wave is much shorter than the growth time of the onset instability, which can be commonly met in practice.
2) Time dependent oscillation variables except for velocity, such as the fluctuation pressure, temperature, etc., are much smaller than their average values. The time dependent oscillating velocity is much smaller than the speed of sound.
3) Linear temperature profile is assumed along the regenerator and thermal buffer tube. Axial thermal conductions through the regenerator matrix and the walls are ignored.
4) The source term arising from the temperature gradient of the thermal buffer tube is considered to be small enough to be ignored in the continuity equation.
5) The elastic membrane is not included in the model. The cavities above and below the membrane are all treated as ducts with the same diameter as that of the compliance.
6) Laminar flow is assumed during the whole onset process.
7) No acoustic streaming occurs in the system.

TABLE 1. Geometric parameters of traveling-wave thermoacoustic engine and the grid number used in computation.

Component	Inner Diameter/m	Length/m	Grids
Tube1	0.09	0.126	3
2rd AHX	0.09	0.02	1
Thermal buffer	0.1	0.291	7
HHX	/	0.12	2
Regenerator	0.09	0.074	10
AHX	/	0.056	2
Compliance	0.1	0.6767	10
Cone1	/	0.1	2
Inertance tube	0.076	0.28	6
Cone2	/	0.095	2
Tube2	0.09	0.295	5
Tube3	0.09	0.095	2
Cone3	/	0.1	2
Resonator	0.1	2.3	20
Cone4	/	1.31	11
Reservoir	0.261	0.52	5

2.2.1. Ducts and heat exchangers

The duct components include the compliance tube, inertance tube, resonator, reservoir, and the connecting tubes, etc. As the hydraulic radius is much larger than the thermal penetration depth in the thermal buffer tube, the source term caused by the temperature gradient is ignored in the continuity equation for simplicity. Thus, it shares the same governing equations with other duct components. Heat exchangers are assumed at fixed temperatures uniformly and also have the same forms of governing equations.

Every oscillating variable can be written as the combination of the mean and time-dependent fluctuation terms. With the assumption that the period of pressure wave is much shorter than the developing time of the onset process and accepting Rott's approximation [16], the fluctuation terms can be further written in the complex notations as follows

$$p(x,t) = p_0 + p'(x,t) = p_0 + \text{Re}[p_1(x)e^{i\omega t}] \,, \tag{1}$$

$$u(x,y,z,t) = u_0(x) + u'(x,y,z,t) = u_0(x) + \text{Re}[u_1(x,y,z)e^{i\omega t}] \,, \tag{2}$$

$$T(x,y,z,t) = T_0(x) + T'(x,y,z,t) = T_0(x) + \text{Re}[T_1(x,y,z)e^{i\omega t}] \,, \tag{3}$$

$$\rho(x,y,z,t) = \rho_0(x) + \rho'(x,y,z,t) = \rho_0(x) + \text{Re}[\rho_1(x,y,z)e^{i\omega t}] \,, \tag{4}$$

where the subscript 0 and the prime denote mean value and fluctuation term, respectively. The subscript 1 means the first order value of a complex containing the amplitude and phase. No mean flow can occur with the aforementioned assumptions, so $u_0(x) = 0$. The cross-sectional averaged volume flow rate can be calculated by local velocity as follows:

$$U'(x,t) = \int u'(x,y,z,t)dA \,, \tag{5}$$

where A is the cross-sectional area.

Neglecting the second and higher orders, the x axial component of the momentum equation for the flow in a duct is

$$\rho_0 \frac{\partial u'}{\partial t} = -\frac{\partial p'}{\partial x} + \mu \left(\frac{\partial^2 u'}{\partial y^2} + \frac{\partial^2 u'}{\partial z^2} \right).$$

(6)

The left side of the equation is the inertance of the fluid, and the right side is the sum of pressure gradient and the drag term from viscosity. Eq. (6) can be changed into the complex form in the frequency-domain,

$$i\omega \rho_0 u_1 = -\frac{dp_1}{dx} + \mu \left(\frac{\partial^2 u_1}{\partial y^2} + \frac{\partial^2 u_1}{\partial z^2} \right).$$

(7)

Averaging Eq. (7) over the cross-sectional area A gives

$$i\omega \rho_0 \frac{U_1}{A} = -\frac{dp_1}{dx} + \frac{1}{A} \int \left[\mu \left(\frac{\partial^2 u_1}{\partial y^2} + \frac{\partial^2 u_1}{\partial z^2} \right) \right] dA.$$

(8)

Swift [16] used a spatially averaged complex viscous function f_v to characterize the drag effect in linear thermoacoustic theory,

$$\frac{dp_1}{dx} = -i\omega \rho_0 \frac{1-\mathrm{Re}[f_v]}{|1-f_v|^2} \frac{U_1}{A} + \omega \rho_0 \frac{\mathrm{Im}[f_v]}{|1-f_v|^2} \frac{U_1}{A}.$$

(9)

Comparing Eq. (8) with the momentum equation of linear thermoacoustic theory, i.e. Eq. (9), the spatially averaged drag term can be derived,

$$\frac{1}{A} \int \left[\mu \left(\frac{\partial^2 u_1}{\partial y^2} + \frac{\partial^2 u_1}{\partial z^2} \right) \right] dA = \frac{U_1}{A} \left[\omega \rho_0 \frac{\mathrm{Im}[f_v]}{|1-f_v|^2} - i\omega \rho_0 \left(\frac{1-\mathrm{Re}[f_v]}{|1-f_v|^2} - 1 \right) \right].$$

(10)

Transforming Eq. (10) back into the time-domain form yields

$$\frac{1}{A} \int \left[\mu \left(\frac{\partial^2 u'}{\partial y^2} + \frac{\partial^2 u'}{\partial z^2} \right) \right] dA = \left[\frac{\omega \rho_0}{A} \frac{\mathrm{Im}[f_v]}{|1-f_v|^2} U' - \frac{\rho_0}{A} \left(\frac{1-\mathrm{Re}[f_v]}{|1-f_v|^2} - 1 \right) \frac{\partial U'}{\partial t} \right].$$

(11)

As shown in the above equation, the drag force arising from viscosity not only has a component in phase with the volume flow, i.e. viscous resistance, but also has one out of phase with the volume flow for oscillating flow [30].

Substituting Eq. (11) into the averaged Eq. (6) over the cross-sectional area A gives the expression of the momentum equation in the time-domain,

$$\frac{\partial p'}{\partial x} = -l \frac{\partial U'}{\partial t} - r_v U',$$

(12)

where l and r_v are inertance and resistance of the fluid per unit length,

$$l = \frac{\rho_0}{A} \frac{1-\mathrm{Re}[f_v]}{|1-f_v|^2},$$

(13)

$$r_v = \frac{\omega \rho_0}{A} \frac{\mathrm{Im}[-f_v]}{|1-f_v|^2}.$$ (14)

The continuity equation and the heat transfer equation can be written as

$$\frac{\partial \rho'}{\partial t} + \rho_0 \frac{\partial u'}{\partial x} = 0,$$ (15)

$$\rho_0 c_p \frac{\partial T'}{\partial t} = \frac{\partial p'}{\partial t} + k\left(\frac{\partial^2 T'}{\partial y^2} + \frac{\partial^2 T'}{\partial z^2}\right).$$ (16)

The left side of the Eq. (16) denotes the heat capacity of the fluid, and the right side denotes the thermal effects from the pressure oscillation and heat transfer, respectively.

The state equation of ideal gas is

$$\frac{1}{\rho_0} d\rho' = -\frac{1}{T_0} dT' + \frac{1}{p_0} dp'.$$ (17)

Substituting Eq. (17) into Eq. (15) yields,

$$-\frac{1}{T_0} \frac{\partial T'}{\partial t} + \frac{1}{p_0} \frac{\partial p'}{\partial t} + \frac{\partial u'}{\partial x} = 0.$$ (18)

Substituting Eq. (16) into Eq. (18) with the time deviation of temperature, and averaging over the cross-sectional area A yield

$$-\frac{1}{\rho_0 c_p T_0}\left[\frac{\partial p'}{\partial t} + \frac{1}{A}\int k\left(\frac{\partial^2 T'}{\partial y^2} + \frac{\partial^2 T'}{\partial z^2}\right)dA\right] + \frac{1}{p_0}\frac{\partial p'}{\partial t} + \frac{1}{A}\frac{\partial U'}{\partial x} = 0.$$ (19)

Transforming the above equation into complex form, and substituting the relation of $\rho_0 c_p T_0 = p_0 \gamma / (\gamma - 1)$ yield

$$\frac{1}{A}\int k\left(\frac{\partial^2 T_1}{\partial y^2} + \frac{\partial^2 T_1}{\partial z^2}\right)dA = \frac{i\omega p_1}{\gamma-1} + \frac{\gamma p_0}{\gamma-1}\frac{1}{A}\frac{dU_1}{dx}.$$ (20)

In linear thermoacoustic theory, the continuity equation for ducts without temperature gradient is [16],

$$\frac{1}{A}\frac{dU_1}{dx} = -\frac{i\omega}{\gamma p_0}\left[1 + (\gamma-1)f_\kappa\right]p_1.$$ (21)

Similar to the derivation of the averaged drag term in the momentum equation, the averaged heat transfer term can be expressed as the spatially averaged complex thermal function f_κ by comparing the Eqs. (20) and (21),

$$\frac{1}{A}\int k\left(\frac{\partial^2 T'}{\partial y^2} + \frac{\partial^2 T'}{\partial z^2}\right)dA = -\mathrm{Re}[f_\kappa]\frac{\partial p'}{\partial t} + \omega\,\mathrm{Im}[f_\kappa]p'.$$ (22)

Substituting Eq. (22) into Eq. (19) gives the expression for the continuity equation in the time-domain,

$$\frac{\partial U'}{\partial x} = -c\frac{\partial p'}{\partial t} - \frac{1}{r_\kappa}p', \tag{23}$$

where c and r_κ are the compliance and thermal-relaxation resistance of the fluid per unit length,

$$c = \frac{A}{\gamma p_0}\left(1+(\gamma-1)\mathrm{Re}[f_\kappa]\right), \tag{24}$$

$$r_\kappa = \frac{\gamma}{\gamma-1}\frac{p_0}{\omega A \mathrm{Im}[-f_\kappa]}. \tag{25}$$

The complex functions f_ν and f_κ depend on the geometry of the gas channel. For circular tubes with diameter $D=4r_h$, where r_h is the hydraulic radius, such as ducts and AHXs,

$$f_{\kappa,\nu} = \frac{4J_1[0.5(i-1)D/\delta_{\kappa,\nu}]}{J_0[0.5(i-1)D/\delta_{\kappa,\nu}](i-1)D/\delta_{\kappa,\nu}}, \tag{26}$$

where $\delta_{\kappa,\nu}$ denotes the thermal penetration depth $\delta_\kappa = \sqrt{2k/\omega\rho c_p}$ or viscous one $\delta_\nu = \sqrt{2\mu/\omega\rho}$. For parallel plates with spacing $2y_0=2r_h$, such as HHX,

$$f_{\kappa,\nu} = \frac{\tanh[(1+i)y_0/\delta_{\kappa,\nu}]}{(1+i)y_0/\delta_{\kappa,\nu}}. \tag{27}$$

2.2.2. Regenerator

One-dimensional momentum equation of compressible fluid flow is

$$\frac{\partial(\rho u')}{\partial t} + \frac{\partial(\rho u'^2)}{\partial x} + \frac{\partial p'}{\partial x} + \frac{1}{2}\frac{f}{r_h\phi^2 A^2}\rho_0|U'|U' = 0, \tag{28}$$

where f, r_h and ϕ are the friction factor, hydraulic radius and porosity of the regenerator, respectively.

Ignoring the second and higher order terms, and taking into account of the effect of the tortuosity of the flow path through the screen mesh on the inertance term by introducing a factor c_1 [16], the above momentum equation can be expressed as

$$\frac{\partial p'}{\partial x} = -\frac{\rho_0 c_1}{\phi A}\frac{\partial U'}{\partial t} - \frac{1}{2}\frac{f}{r_h\phi^2 A^2}\rho_0|U'|U', \tag{29}$$

The first and second terms of the RHS are the inertial and dissipative contributions to the pressure gradient. The friction factor of the screen type regenerator can be writen as as a function of the instant Reynolds number R_e [16],

$$f = \frac{c_2}{R_e} + c_3. \tag{30}$$

where $R_e = 4|U'|r_h\rho_0/(\mu_0\phi A)$. The constants c_1, c_2, and c_3 are the functions of the porosity ϕ [31]:

$$c_1 = 1+(1-\phi)^2/2(2\phi-1), \quad c_2 = 1268-3545\phi+2544\phi^2, \quad c_3 = -2.82+10.7\phi-8.6\phi^2.$$

The continuity equation can be expressed as

$$\frac{\partial \rho}{\partial t} + \frac{\partial (\rho u')}{\partial x} = 0 . \tag{31}$$

Keeping only the first order terms yields

$$\frac{\partial \rho'}{\partial t} + \rho_0 \frac{\partial u'}{\partial x} + u' \frac{d\rho_0}{dx} = 0 . \tag{32}$$

According to the ideal gas equation of state,

$$\frac{d\rho_0}{dx} = -\frac{\rho_0}{T_0} \frac{dT_0}{dx} + \frac{1}{T_0} \frac{dp_0}{dx} = -\frac{\rho_0}{T_0} \frac{dT_0}{dx} . \tag{33}$$

Substituting Eqs. (33) and (17) into Eq. (32), and averaging over the cross-sectional area gives the continuity equation

$$\frac{\partial U'}{\phi A dx} = \frac{1}{T_0} \frac{\partial T'}{dt} - \frac{1}{p_0} \frac{\partial p'}{dt} + \frac{1}{T_0} \frac{dT_0}{dx} \frac{U'}{\phi A} . \tag{34}$$

The largest terms on the RHS of Eq. (34) are the second and third ones, which represent the isothermal compression and thermal expansion of the working gas as it moves along the temperature gradient, respectively. The first term accounts for the thermal relaxation mechanisms in regenerator caused by finite solid specific heat and imperfect heat transfer, which is thought to be much smaller than the other two terms. Although the first term is relatively small, it represents the power dissipation by the thermal relaxation in the regenerator, so it may cause noticeable deviations to ignore it particularly when we focus on the dynamic onset process. Two different models are then adopted to investigate the influence of the thermal relaxation term. Model A uses the continuity equation in the form of Eq. (34), with the first term ignored. To reach a solution at this stage to the very stubborn issue of taking thermal relaxation into account, a compromise is made here to adopt a different continuity equation derived from linear thermoacoustic theory [16] in the following form, which is called model B,

$$\frac{\partial U'}{\partial x} = -c \frac{\partial p'}{\partial t} - \frac{1}{r_\kappa} p' + \mathrm{Re}[g]U' + \frac{\mathrm{Im}[g]}{\omega} \frac{\partial U'}{\partial t} , \tag{35}$$

where g is the complex source term,

$$g = \frac{f_\kappa - f_\nu}{(1 - f_\kappa)(1 - \mathrm{Pr})} \frac{1}{T_0} \frac{dT_0}{dx} . \tag{36}$$

The derivation process of the above equation is similar to that of Eq. (23). When the temperature gradient is zero, the source term g is zero, and Eq. (35) simply becomes Eq. (23), which is the continuity equation for tubes. For traveling-wave thermoacoustic engines, the thermal contaction between gas and screen solid in regenerator is relatively good, and the source term g approaches $dT_0/(T_0 dx)$, which means that the volume flow rate is amplified in proportion to the temperature ratio. For stacked screens and other non-uniform geometries, the thermal and viscous functions can be determined empirically [32]. In the present study, the complex functions f_κ and f_ν of regenerators are calculated approximately with Eq. (26) by using the hydraulic radius as the input value.

2.3. Discretization method and numerical algorithm

According to the above governing equations of the duct and heat exchanger components, the pressure gradient is caused by the inertance and resistance effects of the fluid, and the volume flow gradient is caused by the compliance and thermal-relaxation effects. For the regenerator, the volume flow is mainly affected by the compliance effect and temperature gradient. As a result, the traveling-wave thermoacoustic engine can be made equivalent to the network model shown Fig. 2. The pistons with mechanical resistances represent the acoustic inertances and resistances, and the lossy volumes between the pistons represent the compliance and thermal-relaxation effects. The discretized governing equations for acoustic ducts and heat exchangers in the models A and B can be expressed as

$$\frac{dU'_i}{dt} = -\frac{1}{l_i dx_i}\left(p'_i - p'_{i-1} + r_{v,i} dx_i U'_i\right),$$ (37)

$$\frac{dp'_i}{dt} = -\frac{1}{c_i dx_i}\left(U'_{i+1} - U'_i + \frac{1}{r_{\kappa,i}} dx_i p'_i\right),$$ (38)

where i denotes the node number of acoustic ducts and heat exchangers.

The momentum equation for the regenerator in the models A and B are both discretized as

$$\frac{dU'_j}{dt} = -\frac{\phi A_j}{\rho_{0,j} c_1 dx_j}\left(p'_j - p'_{j-1} + \frac{\rho_{0,j}|U'_j| f_j dx_j}{2r_h \phi_j^2 A_j^2}U'_j\right),$$ (39)

where j denotes the node number of the regenerator.

The discretized continuity equation for regenerator in model A is expressed as

$$\frac{dp'_j}{dt} = -\frac{p_0}{\phi A_j dx_j}\left[U'_{j+1} - \left(1 + \frac{dT_{0,j}}{T_{0,j}}\right)U'_j\right],$$ (40)

while in model B,

$$\frac{dp'_j}{dt} = -\frac{1}{c_j dx_j}\left(U'_{j+1} - U'_j + \frac{1}{r_{\kappa,j}} dx_j p'_j - \mathrm{Re}[g_j]U'_j - \frac{\mathrm{Im}[g_j]}{\omega}\frac{dU'_j}{dt}\right),$$ (41)

A set of first-order differential equations can be formed by combining all the governing equations of the grids. The equation set is closed with the conservation equation of the volume flows at the tee joint and the boundary condition of $U'_1 = 0$ at the end of the reservoir. The AHXs and all the tubes except for the thermal buffer tube are set at 283.15 K, which coincides with the experimental condition. The working substance in simulations and experiments is all pure helium gas. Linear temperature distributions are assumed along the regenerator and thermal buffer tube. The physical properties of the helium gas are obtained from Refprop7.1 [33]. The equation set is solved by using the Matlab ODE45 solver with a given initial standing-wave pressure distribution along the system. The highest pressure of the initial pressure profile in the engine is less than 1 Pa. Time step is set as 5×10^{-4} s, which has been proven to be small enough to produce results independent of time step size. An initial angular frequency should be first guessed to calculate the coefficients for the governing equations, and then the calculated oscillation angular frequency, which has been proved to be the converged value, is used in the following iterations to get the final results. To calculate the onset temperature, the temperature of the HHX is adjusted carefully with a very small step during the time when the pressure amplitude at the tee joint remains the same, i.e. the relative change rate of the pressure amplitude in the nearby 12 cycles is within $\pm 5\times10^{-6}$.
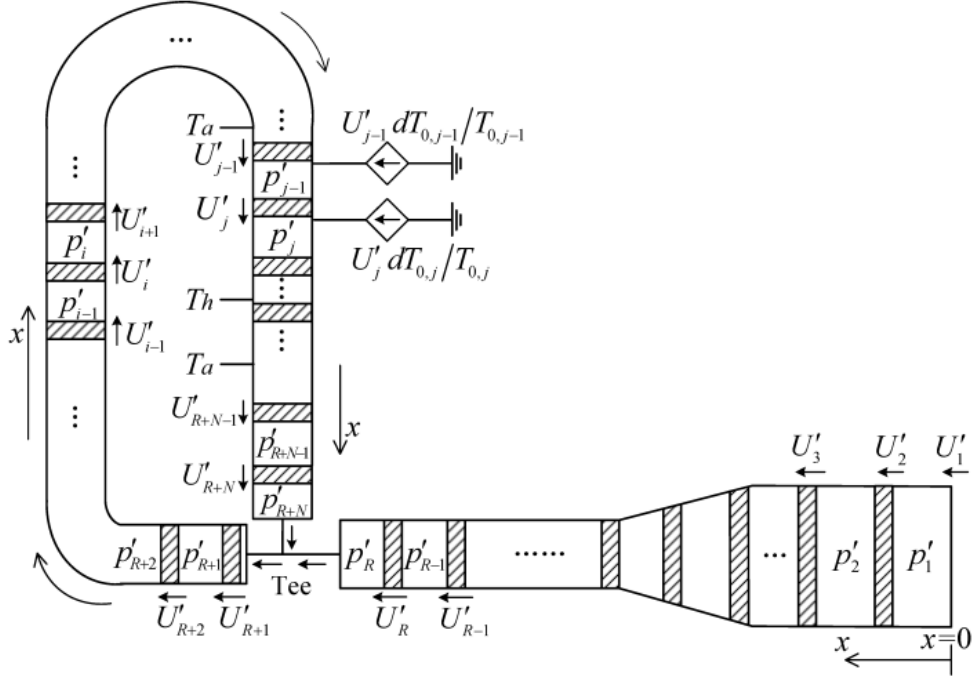
FIG. 2. Schematic of the equivalent discretized network of traveling-wave thermoacoustic engine.

Grid independency validation are performed by using three sets of grid numbers: total number of 90 grids as given in Table 1, 180 grids, and 270 grids. Table 2 shows the calculated onset temperatures at different grid numbers using the models A and B when the mean pressure is 1.8 MPa. It is shown that the onset temperatures for both models vary by less than 0.3%. To save the computation resources with an acceptable accuracy level, the total grid number is set as 90 in both models.

TABLE 2. Calculated onset temperature at 1.8 MPa with different grid numbers.

Total grid number	Onset temperature/K	
	Model A	Model B
90	410.299	420.288
180	411.360	421.355
270	411.393	421.422

3. Numerical results and experimental verifications

Figs. 3-5 show the numerically computed dynamic pressure evolutions at the tee joint and the corresponding spectrum analyses with helium of 1.8 MPa as working gas when the heating temperature T_h is fixed at 380 K, 415 K and 440 K, respectively. As shown in Fig. 3, the initial given pressures both damp in model A and model B when the heating temperature is 380 K, which indicates that the temperature is below the onset temperatures. The acoustic generation is too small to compensate the acoustic losses at this temperature, which leads to the damping processes. The damping rate calculated by model B is quicker than that by model A, which shows more dissipation effect is included in model B. The oscillation frequencies calculated by the two models are the same, which shows the weak influence of the revision of the continuity equation in model B on the frequency.
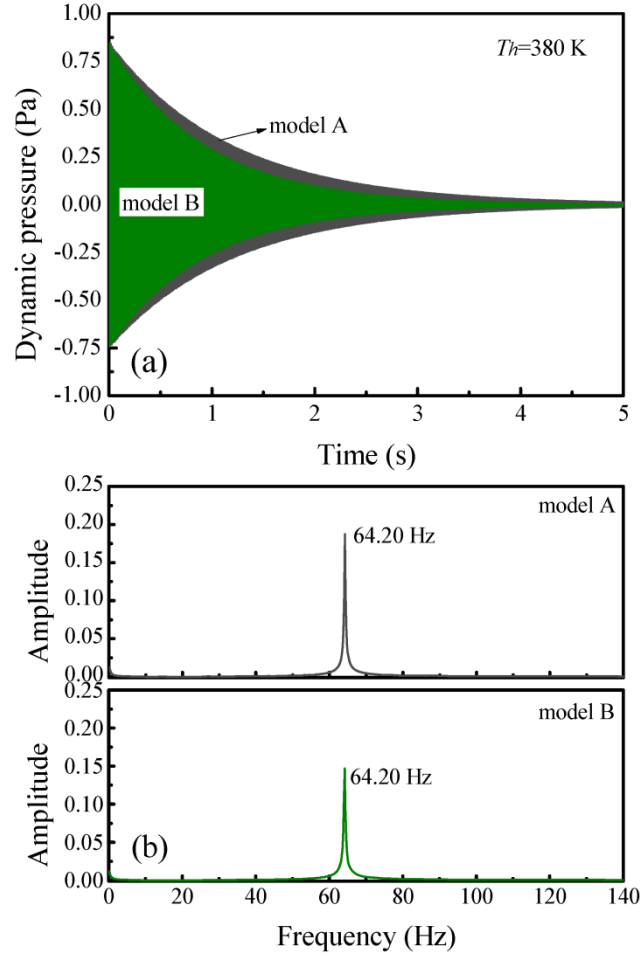
FIG. 3. (Color online) Dynamic pressure evolutions (a) and spectrum diagrams (b) at the tee joint when heating temperature T_h=380 K at 1.8 MPa.

When the heating temperature is 415 K, the calculated dynamic pressure evolutions of models A and B are totally different. The pressure oscillation calculated by model A grows which indicates that the heating temperature has exceeded the onset temperature. Therefore, the onset temperature calculated by model A should be within the range of 380 K and 415 K, and can be further determined by trying new heating temperatures between them and narrowing the range. Different from model A, the pressure oscillation of model B is still damping, which indicates the calculated onset temperature is higher than 415 K. Compared to the damping process shown in Fig. 3, it takes much longer time for the pressure oscillation to approach zero at the higher temperature. The growth or damping of the pressure amplitude becomes slower until no changes occur when the heating temperature is approaching the onset point.

When the heating temperature is increased to 440 K, the calculated pressure oscillations are both amplified, as shown in Fig. 5. The pressure oscillations grow rapidly until the saturation states are reached. The growth rate of the pressure oscillation calculated by model A is much larger than that by model B, and is also higher than that at 415 K. The time needed to complete the onset process are about 30 s and 40 s for the models A and B, respectively. The saturated pressure amplitude obtained by model B is 150.3 kPa, which is much lower compared to that by model A, i.e. 223.6 kPa. The comparisons of the dynamic pressure evolution process and the saturated pressure

amplitudes indicate the remarkable influence of the thermal relaxation in the regenerator on the onset process and the performance of the traveling-wave thermoacoustic system. The spectrum analyses show that the calculated oscillation frequencies are very close to each other, with 64.20 Hz by model A and 64.14 Hz by model B.
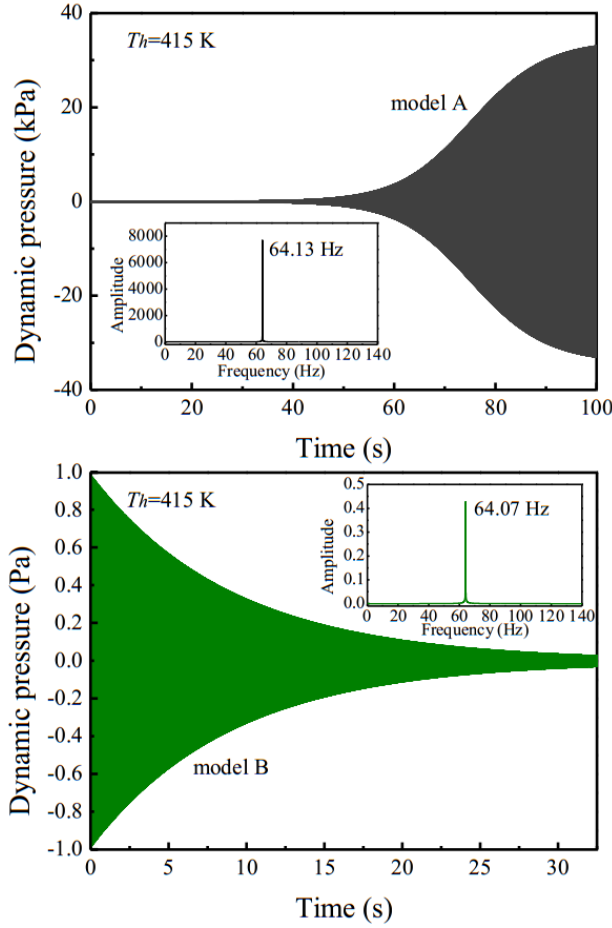

FIG. 4. (Color online) Dynamic pressure evolutions (a) and spectrum diagrams (b) at the tee joint when heating temperature T_h=415 K at 1.8 MPa.

In order to verify the ability of the time-domain models to predict the onset characteristics of traveling-wave thermoacoustic engines, the onset and damping temperatures and the pressure oscillations were measured at various mean pressures with helium as the working gas in the experimental traveling-wave thermoacoustic engine shown in Fig. 1. Calibrated NiCr-NiSi thermocouples were installed to measure the heating temperature T_h at the HHX and the temperatures of the inlet T_{a1} and outlet T_{a2} chilling water at the main AHX. The mean pressure was measured by a piezoresistive pressure sensor with an accuracy of ±0.3%, as denoted by P1 in Fig. 1. The dynamic pressures and frequencies were measured by two PCB piezoelectric pressure sensors (model 102B15), as denoted by P2 and P3. When the frequencies detected by the PCB sensors jumped from zero to a stable resonance frequency, i.e. acoustic oscillation formed, the corresponding heating temperature was determined as the onset temperature. When the heating power was closed, the pressure oscillation weakened gradually as the temperature decreased. If the detected frequencies jumped from the resonance frequency to zero, which meant the pressure oscillation vanished completely, the heating temperature was taken as the damping temperature.
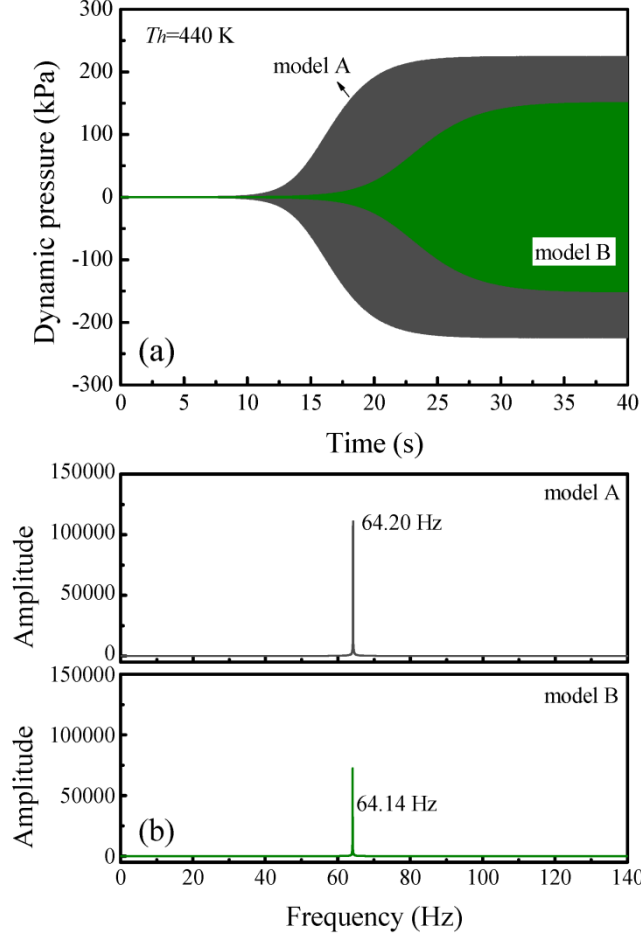
FIG. 5. (Color online) Dynamic pressure evolution (a) and spectrum diagram (b) at the tee joint when heating temperature T_h=440 K at 1.8 MPa.

The calculated onset temperatures at different mean pressures using the models A and B are given in Fig. 6. The experimental results of the onset and damping temperatures are also given for comparison. As shown, the onset temperatures calculated by the models A and B both agree well with the experimental onset temperatures in tendency and magnitude. The deviations between the calculated and experimental onset temperatures are typically around 8.5%~10% for model A, and drop to about 5.8%~9% for model B, which shows that model B is more accurate for predicting the onset temperatures. For example, when the mean pressure is 2.1 MPa, the deviations for the models A and B are 8.53% and 5.87% compared with the experimental results, respectively. When the mean pressure is increased from 2.0 MPa to 3.0 MPa, the onset temperature increases a little in the experiments, while those calculated by model A still decreases a little, and the deviations rise up to about 11%~14.4% at these mean pressures. However, the onset temperature curve obtained by model B, which has taken the thermal relaxation effect into account, always has the same tendency as the experimental results. It means that model B remains plausible even at large mean pressures. The increase of the deviation at higher mean pressures of model A is believed to be mainly caused by neglecting the thermal relaxation effect in the regenerator. The thermal relaxation effect becomes more noticeable at high mean pressures compared to the compliance effect in the regenerator, as apparently shown by their definition equations.

It should be noted that the damping temperature in the experiments is very close to onset

temperature at low mean pressures, but it becomes much lower than the onset one at higher mean pressures. For example, the onset temperature is 460.5 K at 3.0 MPa, while the damping temperature is 436.6 K. As a result, the experimental damping temperatures are much closer to the calculated onset temperatures, and the deviations of them are typically around 6.5%~8% for model A, and only 3.9%~6.5% for model B. The difference between the onset and damping temperatures can be illustrated by the so-called onset-damping hysteresis loop, as reported by previous studies [34]. Unlike the onset process in which the pressure oscillation occurs abruptly and grows sharply, the pressure oscillation weakens gradually during the damping process, and can even be maintained at temperatures much lower than the onset temperature. According to our previous study on the effect of pressure disturbance on the onset temperature and process [35], the onset temperature can be much lower than the ordinary one if an appropriate pressure disturbance is introduced. Therefore, a pressure oscillation may be still maintained and the engine may work at the heating temperatures higher than the damping temperature but lower than the ordinary onset temperature. Since the principle of the numerical calculation of the onset temperature is to determine the lowest temperature at which the pressure oscillation starts to develop, it seems that the damping temperature is the lowest temperature at which the thermoacoustic engine can start to work and maintain the pressure oscillation, which has been verified by our preliminary experiments and will be reported later.
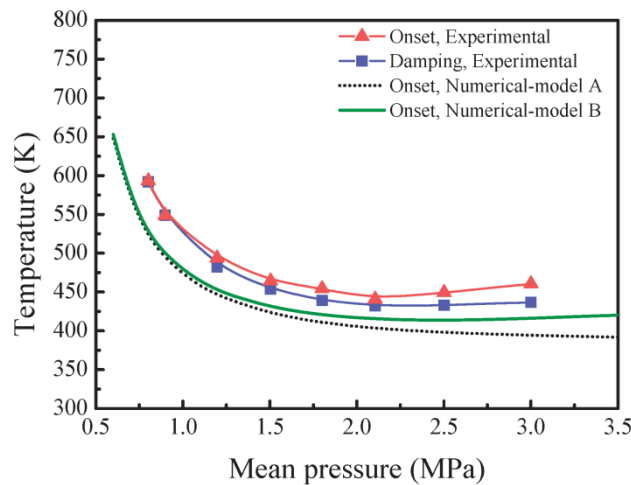

FIG. 6. (Color online) Comparisons between calculated onset temperature and experimental onset and damping temperatures at different mean pressures.

Fig. 7 shows the calculated onset frequencies and the experimental frequencies at different mean pressures. As shown, the onset and damping frequencies in the experiments almost have no noticeable difference and are approximately independent of the mean pressure. The calculated frequencies at different mean pressures of the two models are the same, i.e. 63.97 Hz, which coincides with the experimental results quite well.
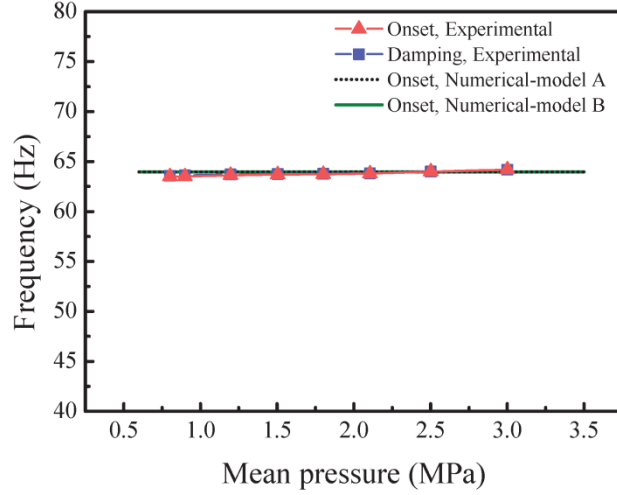
FIG. 7. (Color online) Comparison between calculated and measured onset frequencies at different mean pressures.

The quality factor Q, which is a sensitive probe of energy losses, is defined as the resonant angular frequency ω_0 times the ratio of stored energy E_s to the energy dissipation rate $\dot{E}_d$,

$$Q = \omega_0 \frac{E_s}{\dot{E}_d} . \qquad (42)$$

In a thermoacoustic engine, the stored energy E_s includes the kinetic energy and the potential energy from acoustic oscillations. The energy dissipation rate $\dot{E}_d$ is associated with the viscous, thermal relaxation and other nonlinear effects, except for the acoustic power generation from the regenerator. The aforementioned last one is actually an energy gain rate, which should be denoted as a negative dissipation, when a positive temperature gradient is applied,. The energy dissipation rate decreases and the quality factor increases with the heating temperature as more energy is generated.

Therefore, quality factor is measured and calculated to evaluate the overall performance of the traveling-wave thermoacoustic engine in terms of acoustic energy generation and dissipation. The quality factor Q of the thermoacoustic engine can be determined by fitting the decay curve of pressure oscillation, as shown in Fig. 3, using the following equation [36],

$$p(x,t) = p_0(x) + |p_1(x)| e^{-\frac{\omega_0}{2Q}t} \cos(\omega_0 t + \theta), \qquad (43)$$

where θ is the phase angle of the decaying waveform. A stable acoustic field should be first built up in the thermoacoustic engine by an external excitation before the free decay starts. In the experiments, an electrically driving reciprocating piston was connected to the resonator through a branch composed of a ball valve and a tube at the position of P1, as shown in Fig. 1. The inner diameters of the ball valve and the tube are both 0.05 m. The total length between the equilibrium position of the piston and the connecting point is 0.48 m. Firstly, the piston was reciprocated with a velocity amplitude of 0.5 m/s at the resonant frequency, i.e. about 64 Hz with helium as working gas, to excite the pressure oscillations inside the traveling-wave thermoacoustic engine. When the pressure oscillations became stable, the ball valve was then closed quickly to isolate the engine

from the external excitation source. The pressure oscillation inside the engine started to decay due to the insufficient energy compensation from the thermoacoustic energy conversion to the acoustic power dissipations. The quality factor was then obtained by analyzing the free decay curve. The measurements were repeated three times to get averaged quality factors at different heating temperatures. The measurements and the numerical calculations of the quality factors were conducted on the same traveling-wave thermoacoustic engine as shown in Fig. 1, except that the main AHX was changed a little. In the calculation, the velocity at the end of the branch was first given the same fixed value of 0.5 m/s to excite acoustic oscillation. Then the external excitation was removed, and the velocity at the end of the branch was set as zero, which means a solid end of the branch and is consistant with the experiments. The free damping oscillation was finally obtained numerically with the excited acoustic distributions as the initial inputs. Fig. 8 gives the calculated and measured $1/Q$ at different heating temperatures T_h. When the heating temperature T_h is above the ambient temperature, the acoustic power dissipation in the system is partly compensated by the acoustic power generation in the regenerator due to its thermoacoustic energy conversion effect. The quality factor Q increases with the heating temperature T_h, as more power is generated. As a result, both the experimental and numerical $1/Q$ decrease with the heating temperature, as shown in Fig. 8. The tendencies of the numerical results of models A and B both agree well with the experiments. Comparatively speaking, the results of model B is a little closer to the measurements. When the heating temperature T_h is approaching the onset temperature, the quality factor Q approaches infinite, i.e. $1/Q=0$, because all the power dissipation is compensated by the power generation in the regenerator at this temperature. Both the experimental and numerical onset points are right at the extension of the lines of $1/Q$, as shown by the stars in Fig. 8. The comparisons between the experimental and numerical results show that the models are capable of capturing the characteristics of energy generation and dissipations insides the thermoacoustic system below the onset point.
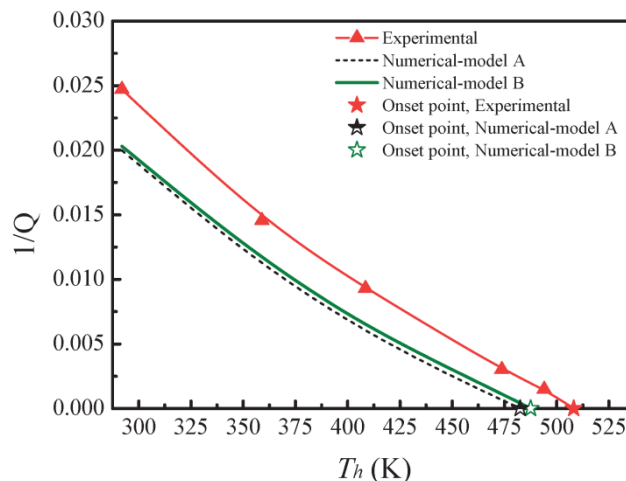

FIG. 8. (Color online) Comparison between calculated and measured $1/Q$ below onset temperature, when mean pressure is 1.8 MPa.

In order to further verify the model, numerical calculations of the onset temperatures and the frequencies are also conducted on a traveling-wave thermoacoustic engine constructed by other researchers [37], in which helium was used as working gas. The comparisons between the numerical and experimental results on the onset temperatures are given in Fig. 9. The numerical models, especially model B, are also able to predict the onset temperature with relatively high

accuracies. The deviations between the calculations and experiments are around 8.5%~10.5% for model A, and only 6.8%~7.8% for model B. The differences between the onset temperatures calculated by the models A and B become larger at higher mean pressures, which further demonstrates the importance of thermal relaxation effect in the regenerator. The calculated frequency is 64.97 Hz, which is close to the experimental one, i.e. about 63 Hz. This little frequency deviation may result from some small differences in dimensions between calculation and experiments [37].
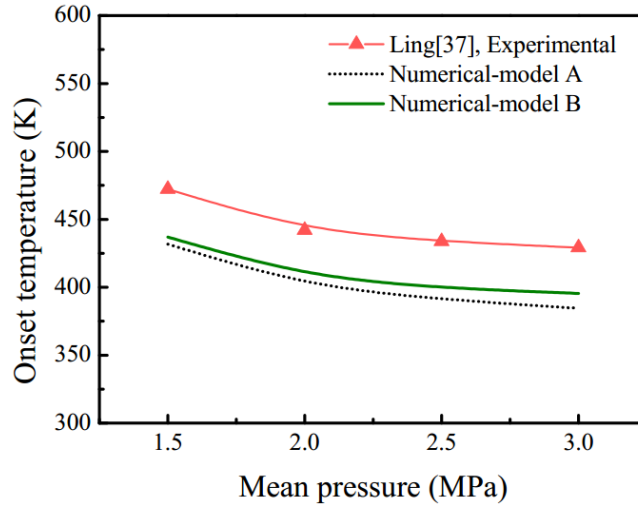

FIG. 9. (Color online) Comparison of onset temperatures between computation and Ling's [37] experimental results at different mean pressures.

Although an accurate prediction of high amplitude performance of traveling-wave thermoacoustic engines is out of the scope of the present study, this time-domain model is able to show the distributions of acoustic parameters in the whole thermoacoustic engine reasonably, which further verifies the plausibility of the physical model. Thus, the calculated pressures, volume flow rates, and phase differences are hereinafter presented and analyzed.

Figs. 10-11 show the waveforms of the dynamic pressures and the volume flow rates at the ambient and hot ends of the regenerator after 40 s calculation using model B when the heating temperature is 440 K and the mean pressure is 1.8 MPa. As shown, the waveforms are of good sinusoidal shapes. The phase differences between the dynamic pressure and volume flow rate are
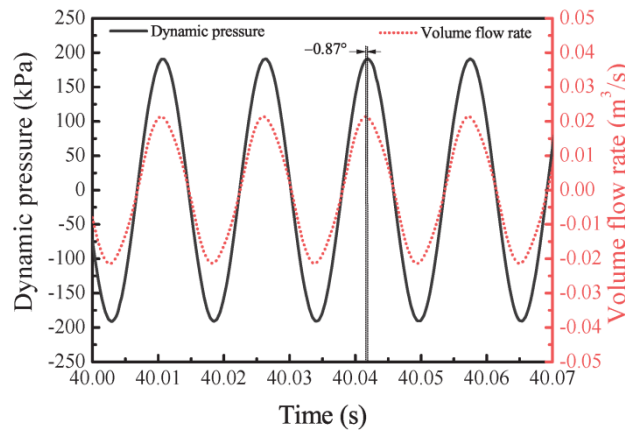

FIG. 10. (Color online) Waveforms of dynamic pressure and volume flow rate at the ambient end of regenerator after 40 s calculation using model B.
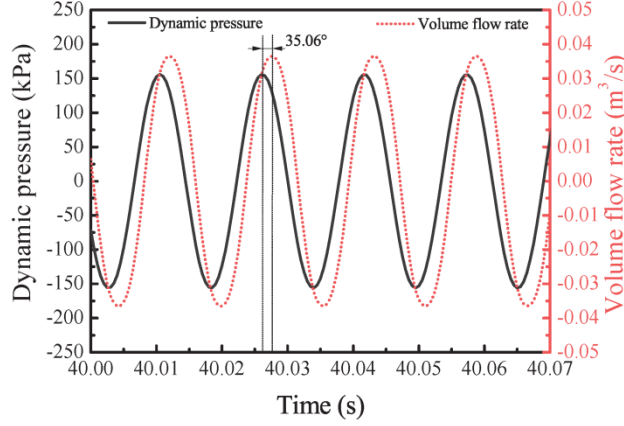
17

FIG. 11. (Color online) Waveforms of dynamic pressure and volume flow rate at the hot end of regenerator after 40 s calculation using model B.

−0.87° and 35.06°, respectively, which shows that the regenerator works at a near traveling-wave phase angle. The pressure amplitude at the hot end is smaller than that at the ambient end mainly due to the viscous resistance in the regenerator. On the contrary, due to the remarkable temperature gradient in the regenerator, the amplitude of volume flow rate at the hot end is much higher than that at the ambient end, which results in the power gain of the regenerator.

The distributions of the pressure and volume flow rate amplitudes in the whole thermoacoustic engine after 40 s calculation using model B at 440 K are given in Fig. 12. The origin of the coordinate, i.e. $x=0$, is set at the right end of the reservoir, as shown Fig. 1 and Fig. 2. The positive direction of x is shown by the arrows. As shown, the pressure and the volume flow rate amplitudes are of near standing-wave acoustic field distributions in the resonator part. The amplitude of volume flow rate reaches the maximum in the resonator near the connecting point between the resonator and the cone 4, where the pressure node also occurs. The volume flow from the resonator is divided into two parts at the tee joint, and goes into the torus in two different directions. Thus, a discontinuity in the volume flow amplitude occurs in Fig. 12. The pressure amplitude reaches the maximum right above the regenerator. The pressure amplitude then decreases a lot across the regenerator, as analyzed above. The amplitude of volume flow rate in the regenerator is kept at the lowest level in the system, which is critical to reach a good performance as the viscous loss is suppressed greatly.
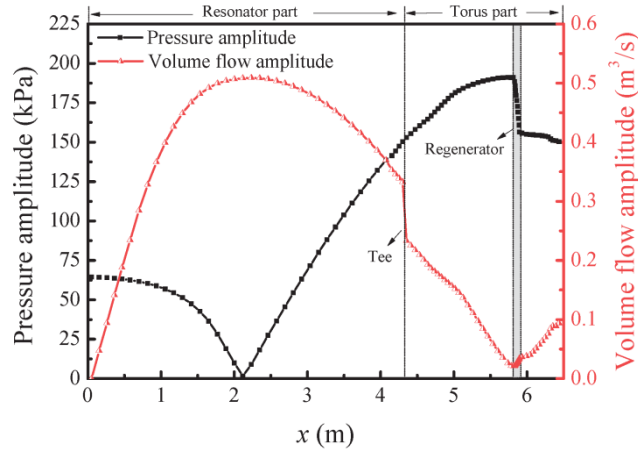

FIG. 12. (Color online) Distributions of pressure and volume flow amplitudes in traveling-wave thermoacoustic engine after 40 s calculation using model B.

18

Accordingly, the phase distributions of the pressure and the volume flow rate as well as their phase difference are shown in Fig. 13. The phase of pressure rarely changes along the system, i.e. nearly zero phase, except that a phase reversal occurs from the pressure node to the end of reservoir. The phase of the volume flow rate in the resonator is all the way nearly at 90°, and the phase difference in the resonator is always at about 90° or −90°, which indicates that the acoustic field in the resonator is nearly a pure standing-wave one. A small discontinuity of the phase of the volume flow rate and the phase difference occur at the tee joint due to the volume flow division. The phase of the volume flow rate and the phase difference change a lot along the torus. The sharpest variations occur from 5.5 m to about 6 m, which is from the middle point of the compliance to the hot end of the regenerator. The phase difference in the torus changes from about −83° to 71° across the zero phase right at the ambient end of the regenerator, generating an appropriate traveling-wave phase relationship for efficient energy conversion. The phase difference behind the pressure node is almost the reversal of the phase of the volume flow rate because of the very small phase value of the pressure. All the physical parameters calculated by model A have similar trends and relationships to those obtained by model B, and are not illustrated for brevity. The main features of the system obtained by the models A and B, such as the characteristics of the distributions of the pressure and volume flows along with the phase difference all agree with those of a practical traveling-wave thermoacoustic engine [16] as well as other numerical results [28,38], which shows the plausibility of the models.
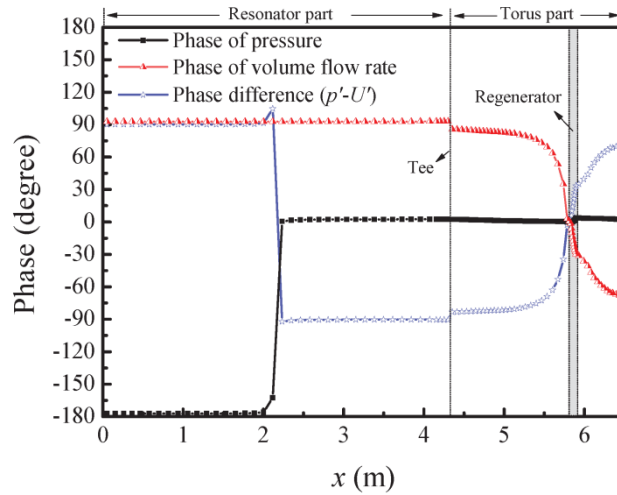

FIG. 13. (Color online) Distributions of phases of pressure and volume flow rate as well as their difference in traveling-wave thermoacoustic engine after 40 s calculation using model B. Pressure phase at the first node of the main AHX, i.e. x=5.786 m, is set at zero as the benchmark. Phase difference is defined as the pressure phase minus the volume flow rate phase.

It is worth noting that the calculated saturated pressure amplitudes are much higher than that measured in experiments under similar conditions. For example, when the heating temperature is 440 K which is about 20 K above the onset temperature calculated by model B, the saturated pressure amplitude of P1 reaches 132.2 kPa. However, the experimental pressure amplitude is only 13.8 kPa when the heating temperature is 20 K above the onset temperature. The very big difference between the calculated and experimental saturated pressure amplitudes is believed to be mainly caused by the severe losses at high pressure amplitude, which exceeds the validation range of linear thermoacoustics. Firstly, the gas flow in the system is assumed to be laminar in the whole onset process, which can only be met at the initial stage of small pressure amplitude. However, large

deviations will occur when the gas flow reaches the turbulence region at higher pressure amplitudes. Secondly, though the thermal relaxation effect in the regenerator is considered in model B, the accurate calculation of it is guaranteed only under small pressure amplitude conditions. Thirdly, the minor losses in the system and the loss from the membrane are not included in the model yet, which are also non-ignorable at high pressure amplitudes. Besides, nonlinear effects which can not be simulated by the model occur at high pressure amplitude and cause extra losses. All in all, the presented model and numerical approach make it more convenient to simulate the energy conversion processes below and just above onset point, and the unstable dynamic oscillations of a thermo-acoustic-mechanical combined system compared to CFD methods [39].

4. Conclusions

A time-domain model for simulating the onset characteristics of traveling-wave thermoacoustic engines is presented. The viscous and heat transfer terms in the momentum and continuity equations of the acoustic ducts and heat exchangers are deduced from linear thermoacoustic theory. Two different models for the regenerator are adopted to evaluate the influence of the thermal relaxation effect on the onset process. The whole pressure evolution process from the onset point is obtained. The experimental verification shows that the model taking into account the thermal relaxation effect is capable of predicting the onset temperatures and quality factors more accurately. Furthermore, it is found that the experimental damping temperature is closer to the calculated onset temperature than the experimental onset temperature, which raises again the unsolved question in this field: which temperature is the lowest temperature required to start a thermoacoustic engine? From this angle, the time-domain models presented here begins to shed a light on the internal onset mechanism of thermoacoustic engines. To extend the capability of the model for accurately predicting the performances of traveling-wave thermoacoustic engines at steady operation states, better treatments of the regenerator and heat exchangers, and taking into account the turbulences and other nonlinear losses should be conducted in the future work.

References

1. Backhaus S., Swift G.W. *A thermoacoustic Stirling heat engine.* Nature, **399**: 335-338 (1999).
2. Wheatley J., Hofler T., Swift G.W., Migliori A. *Experiments with an Intrinsically Irreversible Acoustic Heat Engine.* Physical Review Letters, **50**(7): 499-502 (1983).
3. Sun D.M., Wang K., Xu Y., Shen Q., Zhang X.J., Qiu L.M. *Thermoacoustic compression based on alternating to direct gas flow conversion.* Journal of Applied Physics, **111**: 094905 (2012).
4. Babaei H., Siddiqui K. *Modified theoretical model for thermoacoustic couples.* International Journal of Thermal Sciences, **50**(2): 206-213 (2011).
5. Zoontjens L., Howard C.Q., Zander A.C., Cazzolato B.S. *Numerical study of flow and energy fields in thermoacoustic couples of non-zero thickness.* International Journal of Thermal

Sciences, **48**(4): 733-746 (2009).

6. Piccolo A., Pistone G. *Computation of the time-averaged temperature fields and energy fluxes in a thermally isolated thermoacoustic stack at low acoustic Mach numbers.* International Journal of Thermal Sciences, **46**(3): 235-244 (2007).

7. Mahmud S., Fraser R.A. *Influence of a magnetic field on a single-plate thermoacoustic system.* International Journal of Thermal Sciences, **45**(1): 29-40 (2006).

8. Boroujerdi A.A., Ziabasharhagh M. *Investigation of a high frequency pulse tube cryocooler driven by a standing wave thermoacoustic engine.* Energy Conversion and Management, **86**(0): 194-203 (2014).

9. Wang K., Sun D., Xu Y., Zou J., Zhang X., Qiu L. *Operating characteristics of thermoacoustic compression based on alternating to direct gas flow conversion.* Energy, **75**(0): 338-348 (2014).

10. He Y.L., Ke H.B., Cui F.Q., Tao W.Q. *Explanations on the onset and damping behaviors in a standing-wave thermoacoustic engine.* Applied Thermal Engineering, **58**(1): 298-304 (2013).

11. Yazaki T., Iwata A., Maekawa T., Tominaga A. *Traveling Wave Thermoacoustic Engine in a Looped Tube.* Physical Review Letters, **81**(15): 3128-3131 (1998).

12. Sun D.M., Wang K., Zhang X.J., Guo Y.N., Xu Y., Qiu L.M. *A traveling-wave thermoacoustic electric generator with a variable electric R-C load.* Applied Energy, **106**: 377-382 (2013).

13. Santillan A.O., Boullosa R.R. *Acoustic power and heat fluxes in the thermoacoustic effect due to a travelling plane wave.* International Journal of Heat and Mass Transfer, **40**(8): 1835-1838 (1997).

14. Kang H., Cheng P., Yu Z., Zheng H. *A two-stage traveling-wave thermoacoustic electric generator with loudspeakers as alternators.* Applied Energy, **137**(0): 9-17 (2015).

15. Wu Z.H., Dai W., Man M., Luo E.C. *A solar-powered traveling-wave thermoacoustic electricity generator.* Solar Energy, **86**(9): 2376-2382 (2012).

16. Swift G.W. *Thermoacoustics: A unifying perspective for some engines and refrigerators*, Acoustical Society of America: Sewickley, PA, USA (2002).

17. Yuan H., Karpov S., Prosperetti A. *A simplified model for linear and nonlinear processes in thermoacoustic prime movers. Part II. Nonlinear oscillations.* The Journal of the Acoustical Society of America, **102**(6): 3497-3506 (1997).

18. Karpov S., Prosperetti A. *A nonlinear model of thermoacoustic devices.* The Journal of the Acoustical Society of America, **112**(4): 1431-1444 (2002).

19. Karpov S., Prosperetti A. *Nonlinear saturation of the thermoacoustic instability.* The Journal of the Acoustical Society of America, **107**(6): 3130-3147 (2000).

20. Hamilton M.F., Ilinskii Y.A., Zabolotskaya E.A. *Nonlinear two-dimensional model for thermoacoustic engines.* The Journal of the Acoustical Society of America, **111**(5): 2076-2086 (2002).

21. Qiu L.M., Lai B.H., Li Y.F., Sun D.M. *Numerical simulation of the onset characteristics in a standing wave thermoacoustic engine based on thermodynamic analysis.* International Journal of Heat and Mass Transfer, **55**(7-8): 2200-2203 (2012).

22. Sun D.M., Wang K., Qiu L.M., Lai B.H., Li Y.F., Zhang X.B. *Theoretical and experimental investigation of onset characteristics of standing-wave thermoacoustic engines based on thermodynamic analysis.* Applied Acoustics, **81**(0): 50-57 (2014).

23. Zink F., Vipperman J., Schaefer L. *CFD simulation of a thermoacoustic engine with coiled resonator.* International Communications in Heat and Mass Transfer, **37**(3): 226-229 (2010).

24. Penelet G., Guedra M., Gusev V., Devaux T. *Simplified account of Rayleigh streaming for the description of nonlinear processes leading to steady state sound in thermoacoustic engines.* International Journal of Heat and Mass Transfer, **55**(21-22): 6042-6053 (2012).

25. Yu G.Y., Dai W., Luo E.C. *CFD simulation of a 300 Hz thermoacoustic standing wave engine.* Cryogenics, **50**(9): 615-622 (2010).

26. Tourkov K., Zink F., Schaefer L. *Thermoacoustic sound generation under the influence of resonator curvature.* International Journal of Thermal Sciences, **88**(0): 158-163 (2015).

27. Lycklama à Nijeholt J.A., Tijani M., Spoelstra S. *Simulation of a traveling-wave thermoacoustic engine using computational fluid dynamics.* The Journal of the Acoustical Society of America, **118**(4): 2265-2270 (2005).

28. Yu G.Y., Luo E.C., Dai W., Hu J.Y. *Study of nonlinear processes of a large experimental thermoacoustic-Stirling heat engine by using computational fluid dynamics.* Journal of Applied Physics, **102**: 074901 (2007).

29. de Waele A.T.A.M. *Basic treatment of onset conditions and transient effects in thermoacoustic Stirling engines.* Journal of Sound and Vibration, **325**(4-5): 974-988 (2009).

30. Watanabe M., Prosperetti A., Yuan H. *A simplified model for linear and nonlinear processes in thermoacoustic prime movers .1. Model and linear theory.* Journal of the Acoustical Society of America, **102**(6): 3484-3496 (1997).

31. Swift G.W., Ward W.C. *Simple harmonic analysis of regenerators.* Journal of Thermophysics and Heat Transfer, **10**(4): 652-662 (1996).

32. Liu J., Garrett S.L. *Relationship between Nusselt number and the thermoviscous (Rott) functions.* The Journal of the Acoustical Society of America, **119**(3): 1457-1462 (2006).

33. Lemmon E.W., McLinden M.O., Huber M.L. *NIST Reference Fluid Thermodynamic and Transport Properties—REFPROP version 7.1, User's Guide*, NIST Standard Reference Database 23.

34. Chen G.B., Jin T. *Experimental investigation on the onset and damping behavior of the oscillation in a thermoacoustic prime mover.* Cryogenics, **39**(10): 843-846 (1999).

35. Qiu L.M., Sun D.M., Tan Y.X., Yan W.L., Chen P., Zhao L., Chen G.B. *Effect of pressure disturbance on onset processes in thermoacoustic engine.* Energy Conversion and Management, **47**(11-12): 1383-1390 (2006).

36. Rossing T.D. *Springer handbook of acoustics*, Springer (2007).

37. Ling H. *Numerical simulation of thermal and dynamic performance of thermoacoustic engines and their important experimental improvement-Energy-focused traveling-wave thermoacoustic heat engine*. Chinese Academy of Sciences, Doctor degree (2005).

38. Ward B., Clark J., Swift G.W. *Design Environment for Low-amplitude Thermoacoustic Energy Conversion. Version 6.2. Users Guide.* Los Alamos National Laboratory (2008).

39. Wang K., Sun D.M., Guo Y.N., Qiu L.M. *Study on Beating Effect in Thermoacoustic Power Generation System.* Journal of engineering thermophysics, **35**(8): 1488-1492 (2014) (in Chinese).

Nomenclature

A Cross-sectional area, m^2

c Compliance per unit length, m^2/Pa

c_1 Function of porosity, Eq. (29)

c_2 Function of porosity, Eq. (30)

c_3 Function of porosity, Eq. (30)

c_p Specific heat at constant pressure, $J/(kg \cdot K)$

D Diameter, m

e Natural constant

f Friction coefficient

f_κ Spatial averaged thermal function

f_ν Spatial averaged viscous function

g Complex gain factor arising in continuity equation

i $\sqrt{-1}$; node number

Im[] Imaginary part of complex variable

j Node number

J Bessel function

k Thermal conductivity, $W/(m \cdot K)$

l Inertance of fluid per unit length, kg/m^5

p Pressure, Pa

R_e Reynolds number

r Acoustic resistance per unit length, $Pa \cdot s/m^4$

r_h Hydraulic radius, m

Re[] Real part of complex variable

t Time, s

T Temperature, K

u Velocity, m/s

U Volume flow rate, m^3/s

x Coordinate along sound-propagation direction, m

y Coordinate perpendicular to sound-propagation direction, m

z Coordinate perpendicular to sound-propagation direction, m

y_0 Half of the plates spacing, m

ϕ Porosity

θ Phase angle

γ Specific heat ratio

μ Dynamic viscosity, $Pa \cdot s$

ρ Density, kg/m^3

δ Penetration depth, m

ω Angular frequency, rad/s

Subscript

κ Thermal

ν Viscous

0   mean value

1   First order term

Superscript

'   Fluctuation term

Special symbols

|| Magnitude of complex variable